The Recent Star Formation History of GR 8 from Hubble Space Telescope Photometry of the Resolved Stars

Dohm-Palmer, Robbie C.; Skillman, E.~D.; Gallagher, J.; Tolstoy, E.; Mateo, Mario; Dufour, R.~J.; Saha, A.; Hoessel, J.; Chiosi, C.

Published in:
The Astronomical Journal

DOI:
10.1086/300514

Publication date:
1998

THE ASTRONOMICAL JOURNAL, 116:1227–1243, 1998 September

THE RECENT STAR FORMATION HISTORY OF GR 8 FROM *HUBBLE SPACE TELESCOPE* PHOTOMETRY OF THE RESOLVED STARS[1]

ROBBIE C. DOHM-PALMER AND E. D. SKILLMAN
Department of Astronomy, University of Minnesota, 116 Church Street, SE, Minneapolis, MN 55455; robbie@astro.spa.umn.edu, skillman@astro.spa.umn.edu

J. GALLAGHER
Department of Astronomy, University of Wisconsin, 475 North Charter Street, Madison WI 53706-1582; jsg@jayg.astro.wisc.edu

E. TOLSTOY
Space Telescope European Coordinating Facility, ESO, Karl-Schwarzschild-Strasse 2, D-85748 Garching bei München, Germany; etolstoy@eso.org

MARIO MATEO
Department of Astronomy, University of Michigan, 821 Dennison Building, Ann Arbor, MI 48109-1090; mateo@astro.lsa.umich.edu

R. J. DUFOUR
Department of Space Physics and Astronomy, Rice University, Box 1892, Room 232, Space Sciences Building, Houston, TX 77251-1982; rjd@regulus.rice.edu

A. SAHA
National Optical Astronomy Observatories, 950 North Cherry Avenue, P.O. Box 26732, Tucson, Arizona 85726; saha@noao.edu

J. HOESSEL
Department of Astronomy, University of Wisconsin, 475 North Charter Street, Madison WI 53706-1582; hoessel@jth.astro.wisc.edu

AND

C. CHIOSI
Dipartimento di Astronomia, Università di Padova, vicolo dell'Osservatorio 5, I-35122 Padova, Italy; chiosi@astrpd.pd.astro.it
Received 1998 April 13; revised 1998 June 5

ABSTRACT

We have used the *Hubble Space Telescope* to observe the resolved stars in the dwarf irregular galaxy GR 8 (DDO 155, UGC 8091). The data consisted of dithered Wide Field Planetary Camera 2 images in three bands: F439W (1 hr), F555W (30 minutes), and F814W (30 minutes). The stellar photometry was extracted with a modified version of DoPHOT. Artificial star tests showed the data to be 50% complete to $V = 26.3$, $B = 25.4$, and $I = 25.2$. The color-magnitude diagrams contain well-defined populations, including a very young main sequence (MS) (<10 Myr), and a red giant branch as old as several Gyr. These features align well with stellar evolution models of the appropriate metallicity. The distance based on the tip of the red giant branch is in excellent agreement with the Cepheid determination of $\mu = 26.75 \pm 0.35$ (2.2 Mpc), which we adopted. An extended stellar "halo" was discovered well beyond the H I. Based on the MS and blue HeB luminosity function, we calculated the star formation rate (SFR) over the past 500 Myr. The SFR has been fairly constant, at 400 $M_\odot$ Myr^{-1} kpc^{-2} with up to 60% variations. The blue HeB stars were used as a tracer for the location of star formation over this time period. The star formation occurred in superassociation size regions (100–200 pc), which lasted $\sim$100 Myr. These regions come and go with no obvious pattern, except that they seem to concentrate in the current locations of H I clumps. This suggested that the H I clumps are long-lived features that support several star-forming events over time. The most likely explanation is that the star-forming regions are gravitationally bound. We estimated the gas-to-star conversion efficiency to be 6%. We compared our results with those of three other dI galaxies: Sextans A, Pegasus DIG, and Leo A. There is a trend of higher SFR per area with larger $M_{\rm H\,I}/L_B$. Also, the star formation pattern is similar in all four galaxies. Finally, none of the four dI galaxies contained a large starburst, comparable to those in BCD galaxies. Combining the histories of all four galaxies, this implies that less than 5% of dI galaxies are hosting a strong burst of star formation at any given time. Observations of more galaxies are needed to improve this statistic.

Key words: galaxies: individual (GR 8) — galaxies: stellar content — Local Group — stars: evolution — techniques: photometric

[1] Based on observations with the NASA/ESA *Hubble Space Telescope*, obtained at the Space Telescope Science Institute, which is operated by the Association of Universities for Research in Astronomy, Inc., under NASA contract NAS 5-26555.

1. INTRODUCTION

Galaxy evolution, as established by nearby dwarfs, is an important link to evolutionary models based on high-redshift observations. The large number of "faint blue galaxies" in the redshift range $0.3 < z < 1$ (e.g., Tyson 1988; Koo & Kron 1992; Colless et al. 1993) are commonly assumed to be the precursors for nearby dwarfs (Babul & Ferguson 1996; Spaans & Norman 1997; Campos 1997). The validity of this assumption can be directly tested by calculating the star formation history from the stellar populations in nearby dwarfs. This would establish a direct link between the star formation process and high-redshift galaxies, where this process cannot be seen directly.

GR 8 (DDO 155, UGC 8091) is a gas-rich dI with active star formation. Located at $12^h58^m9^s$, $+14°28'53''$ (J2000.0) ($l = 310.°72$, $b = 76.°98$), it is well above the Galactic plane. It has a low surface brightness with apparent magnitude $m_V = 14.35 \pm 0.05$ and an extremely blue color of $B-V = 0.26 \pm 0.05$ (Gallagher & Hunter 1986).

There are 32 cataloged H II regions (Hodge, Lee, & Kennicutt 1989). Initially, a very low oxygen abundance (3% Solar) was reported (Skillman et al. 1988a), which made GR 8 a critical point in the M_B-to-O/H relation (Skillman, Kennicutt, & Hodge 1989). This was later revised to a slightly higher value (5% Solar; Moles, Aparicio, & Masegosa 1990), which has been confirmed (Skillman, Kobulnicky, & Dohm-Palmer 1998). Active star formation suggests that molecular gas is present. However, CO has not been detected in GR 8 (Verter & Hodge 1995), which is not surprising, given its low metallicity.

The H I distribution has a horseshoe shape, with a deficit over the northeast end of the galaxy (Carignan, Beaulieu, & Freeman 1990). It is not clear if the H I is rotating (see review by Skillman 1996). Carignan et al. (1990) interpreted the velocity field as rotation, while Lo, Sargent, & Young (1993) found it most consistent with expansion or contraction. Hoffman et al. (1996) found a velocity field consistent with rotation, but with the rotation axis aligned with the optical minor axis. If the galaxy is rotating, the peak rotation velocity is of the same order as the velocity dispersion (6.0 ± 1.2 km s^{-1}; Lo et al. 1993).

The distance to GR 8 has recently undergone a major revision. GR 8 was first observed by Reaves (1956) as part of a dwarf galaxy survey in the Virgo Cluster, and later cataloged as DDO 155 by van den Bergh (1959). Hodge (1974) first discovered that GR 8 was closer than the Virgo Cluster, and estimated the distance to be 0.5 to 1.5 Mpc. The size of the largest H II region, and the brightest stars in the galaxy, indicated GR 8 was 1.05 Mpc away (de Vaucouleurs & Moss 1983; Moss & de Vaucouleurs 1986). Comparison of the color-magnitude diagram (CMD) with that of Sextans A and the Pegasus DIG led Hoessel & Danielson (1983) to estimate the distance at 1.4 Mpc. The first and only primary distance indicator was a single Cepheid measured by Tolstoy et al. (1995). This indicated a distance between 1.9 and 2.6 Mpc ($m - M = 26.75 \pm 0.35$). For this paper, we adopted 2.2 Mpc. As will be discussed in a later section, this value is consistent with our new observations.

There have been several photometric studies of the stellar population. De Vaucouleurs & Moss (1983) measured the brightest 17 stars in the Johnson B passband. Hoessel & Danielson (1983) obtained CCD photometry in g and r (Thuan & Gunn 1976). Aparicio, García-Pelayo, & Moles (1988; hereafter AGM) obtained Johnson UBV photometry down to a limiting magnitude of $V \approx 24$. Hopp & Schulte-Ladbeck (1995; hereafter HS) also presented ground-based optical observations. Far-ultraviolet stellar photometry from *Hubble Space Telescope* (*HST*) Faint Object Camera imaging was measured by Patterson, Wyatt, & Dufour (1993). Finally, Wide-Field/Planetary Camera 1 (WF/PC-1) images were obtained by Wyatt & Dufour (1993), who measured Johnson UBV and Cousins RI photometry of the brightest stars.

In the next section, we present the photometry extraction and calibration. We then discuss the necessary physical parameters needed to interpret the CMDs. The observations are compared with stellar evolution models, followed by calculations of the SFH. Finally, the results are compared with previous work and other dI galaxies, and the implications for dwarf galaxy evolution are discussed.

2. STELLAR PHOTOMETRY

The Wide Field Planetary Camera 2 (WFPC2) observations were obtained on 1997 June 17. A summary is provided in Table 1. A true-color image is presented in Figure 1, along with a reproduction of the Digitized Sky Survey image[2] to help orient the reader. The galaxy fit almost entirely onto chips WF3 and WF4. There are three distinct regions containing young, blue stars.

2.1. *Photometry Measurements*

The exposures were dithered by a fractional pixel amount in order to partially compensate for the undersampled point-spread function (PSF) of the WF chips (Burrows 1994). The dithering produced more symmetric and uniform PSF shapes, which aided in distinguishing faint stars from noise (Dohm-Palmer et al. 1997a). The exposures in each filter were aligned to the nearest pixel and co-added. Cosmic rays were detected and corrected during the co-adding. Because the WF PSF is undersampled, true stars will often be flagged as cosmic rays using standard anti-coincidence techniques. We used a detection routine described by Saha et al. (1996), which was developed to preserve true stars in the undersampled images.

The stellar photometry was measured with the PSF fitting program DoPHOT (Schechter, Mateo, & Saha 1993). We used a version optimized for the undersampled PSF of the WF chips (Saha et al. 1996). DoPHOT uses a modified Gaussian expansion as the model PSF. The shape

TABLE 1

CYCLE 5 *HST* WFPC2 OBSERVATIONS OF GR 8: 1997 JUNE 17

Filter	Exposure (s)
F439W.....	2 × 900, 2 × 1100
F555W.....	3 × 600
F814W.....	3 × 600

[2] The Digitized Sky Surveys were produced at the Space Telescope Science Institute under US government grant NAGW-2166. The images of these surveys are based on photographic data obtained using the Oschin Schmidt Telescope on Palomar Mountain and the UK Schmidt Telescope. The plates were processed into the present compressed digital form with the permission of these institutions.

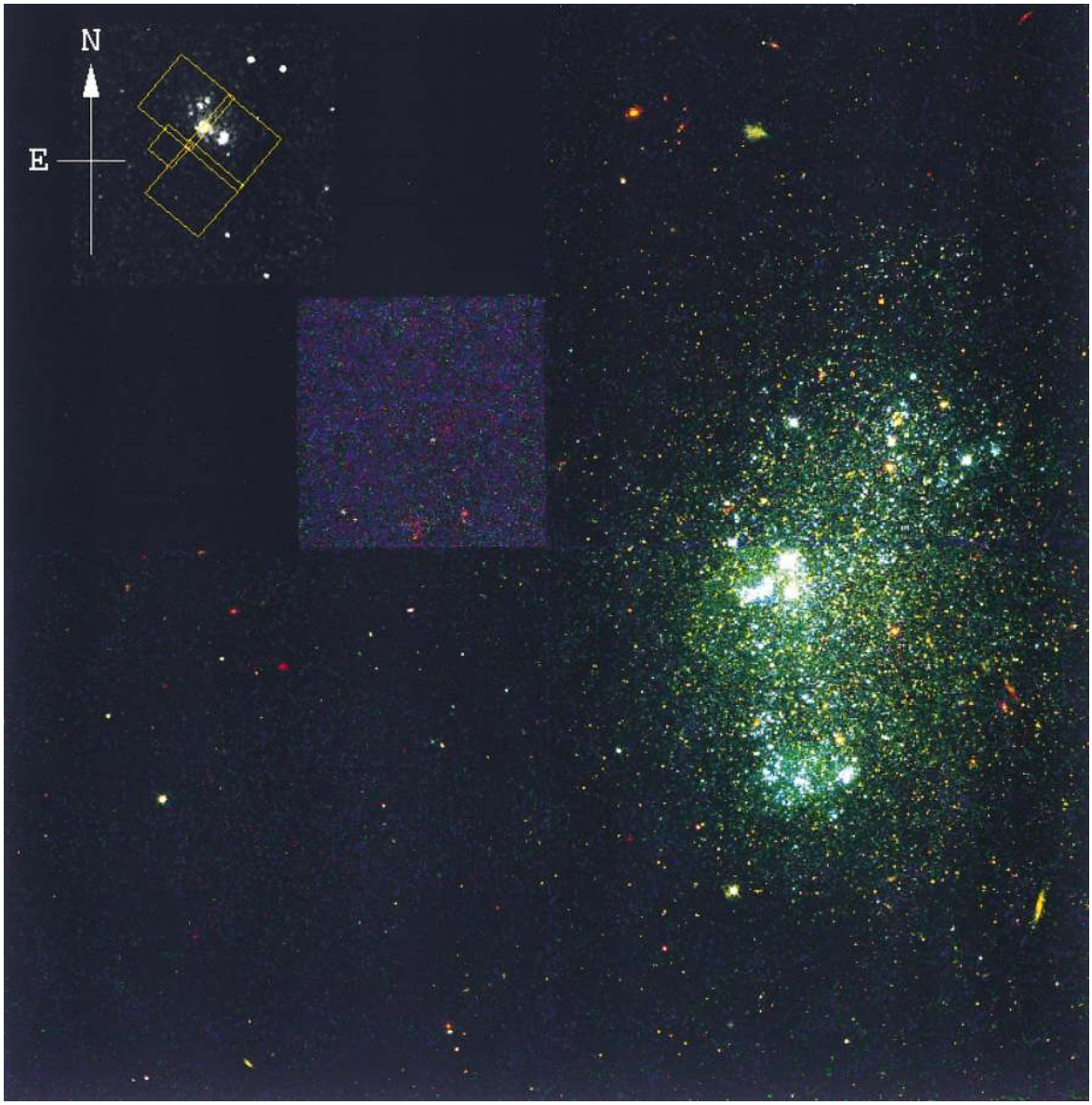

FIG. 1.—True-color reproduction of the *HST* WFPC2 image of the dI galaxy GR 8. The inset in the upper left is the Digitized Sky Survey image with the WFPC2 footprint overlaid. For this inset, north is up and east is to the left. The entire galaxy fits onto chips WF3 and WF4. There are three distinct regions with young blue associations of stars.

can be modified using three parameters: β_4, β_6, and β_8. The shape parameters were determined separately for each filter and chip as follows: Given a set of parameters, the analytic function was fit to 20–30 isolated stars with high signal-to-noise ratios (S/Ns). This fit was subtracted from the image and the rms deviation from the sky background was measured. The shape parameters were varied and this process repeated for each set. The best fit was the set that produced the lowest rms deviation. Table 2 lists the PSF parameters used in our photometry. The values for σ matched well those found for other WFPC2 observations (e.g., Sextans A, Dohm-Palmer et al. 1997a). The β values are not unique in accurately modeling the PSF, so we made no comparisons with other data sets. These numbers are provided for reproducibility.

Aperture corrections were determined for a 0.″5 aperture. The corrections were allowed to vary across the chips to account for a variable PSF. However, the dithering tech-

TABLE 2

DoPHOT Parameters

Chip	σ	β_4	β_6	β_8	Aperture Correction
B:					
1 (PC).....	1.0	1.9	−0.3	0.0	−0.25
2.....	0.8	1.2	1.3	−0.1	−0.21
3.....	0.7	1.8	0.3	0.0	−0.21
4.....	0.7	2.3	−0.8	0.5	−0.23
V:					
1 (PC).....	0.9	2.0	−0.4	0.3	−0.33
2.....	0.6	1.4	0.6	0.0	−0.23
3.....	0.7	1.2	1.4	−0.1	−0.23
4.....	0.6	3.3	−2.0	1.0	−0.16
I:					
1 (PC).....	0.9	4.2	−4.0	1.5	−0.66
2.....	0.7	1.4	0.7	−0.1	−0.44
3.....	0.7	2.6	−2.1	1.3	−0.27
4.....	0.7	2.8	−2.5	1.8	−0.24

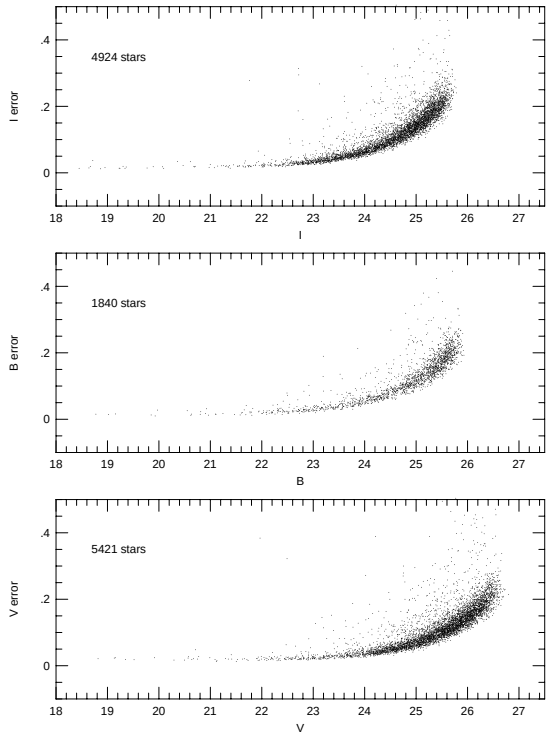

FIG. 2.—Internal measurement errors reported by DoPHOT. The vast majority of the stars lie along a single curve that rises and increases in width toward fainter magnitudes. The highest error on this curve is ~0.25. The scatter of points above this curve comprise only ~1% of the data.

nique produced a very uniform PSF, so a constant correction for each chip was adequate. The aperture corrections are also listed in Table 2.

We searched PC1 and WF2 for stars but found only 3% the number found on WF3 and WF4. There were only a few high-S/N stars from which to determine the PSF shape and the aperture correction for these chips. Given that they contained very few stars, we did not attempt to better define these parameters.

The photometry was transformed from the WFPC2 system to Johnson BV and Cousins I using the transformations given by Holtzman et al. (1995). The internal measurement errors are shown in Figure 2. The vast majority of points are clustered along a curve that both increases to ~0.25 and gets broader toward fainter magnitude. The scatter of points above this curve comprises only ~1% of the stars.

The matching algorithm of Groth (1986) was applied to the brightest 25–30 stars on each chip in order to determine the coordinate transformations between the lists of stars in each filter band. Each list was transformed to a common coordinate system and matched within a specified radius. Stars that had more than one match within this radius were eliminated. To avoid false matches, while not eliminating most of the data, we chose the PSF Gaussian width for the matching radius (see Dohm-Palmer et al. 1997a). Stars were accepted if they were detected in V and at least either B or I.

2.2. *Artificial Star Tests*

Artificial star tests were performed to measure the photometric completeness. Since nearly the entire galaxy fit onto WF3 and WF4, we performed the tests only on these chips. A model PSF was constructed by averaging the shape of 20 to 30 high-S/N stars. Each star was scaled to unity peak intensity and the centroids were aligned. Then, the stars were linearly interpolated and averaged onto a subraster with twice the resolution of the WF chips. Through this linear interpolation the shape was effectively convolved with the sampling pixels. Since the WF chips undersample the PSF, the model was broader than the real stars. We corrected for this broadening by decreasing the model pixel size by the appropriate amount (0.9 in this case) and increasing the pixel intensities to conserve flux (Dohm-Palmer et al. 1997a).

Artificial stars totaling 2% of the real stars were added to 100 frames of each chip and filter. The artificial stars had a uniform distribution in space, and a uniform distribution in $B-V$ and $V-I$ between -1 and 2. The V magnitude was randomly chosen with a power-law distribution that matched the real stars. We added each star to all three filters simultaneously to have consistent colors in the extraction. Finally, we added Poisson noise to each star.

The photometry extraction on each frame was performed identically to that of the true images, including the matching between filters. The recovery lists were matched to the input artificial star lists. This matching radius was 0.5 pixels, so that only detections within one pixel were accepted. Figure 3 shows the fraction of stars recovered in each filter. The dashed line represents the completeness as a function of input magnitude, while the solid line represents the completeness as a function of recovered magnitude. These two are not quite the same because of a form of Malmquist bias (Dohm-Palmer et al. 1997a).

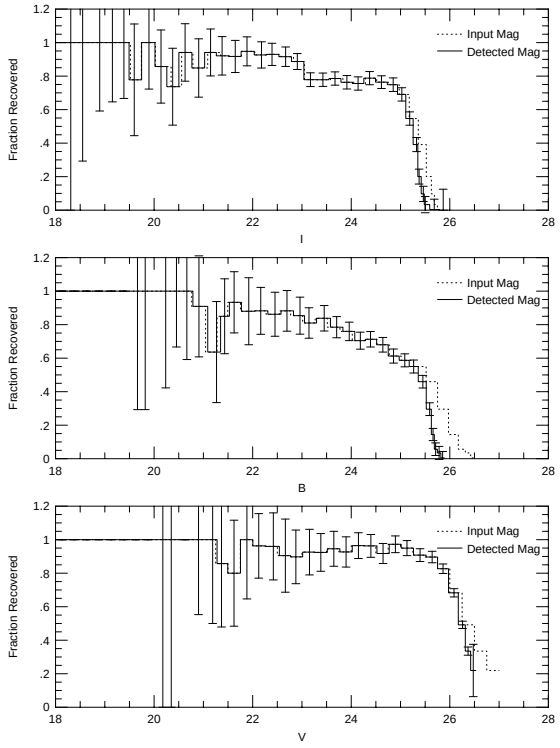

FIG. 3.—Completeness levels of the photometry based on artificial star tests. The dashed line is the completeness level as a function of the input magnitude with 0.25 mag bins. Because of Malmquist bias, we detected some stars with an input magnitude fainter than the detection limits; the noise scatters these stars into brighter magnitudes. The solid line is the histogram corrected to be a function of the detected magnitude. Error bars reflect Poisson counting statistics. The V photometry is the deepest followed by B, then I.

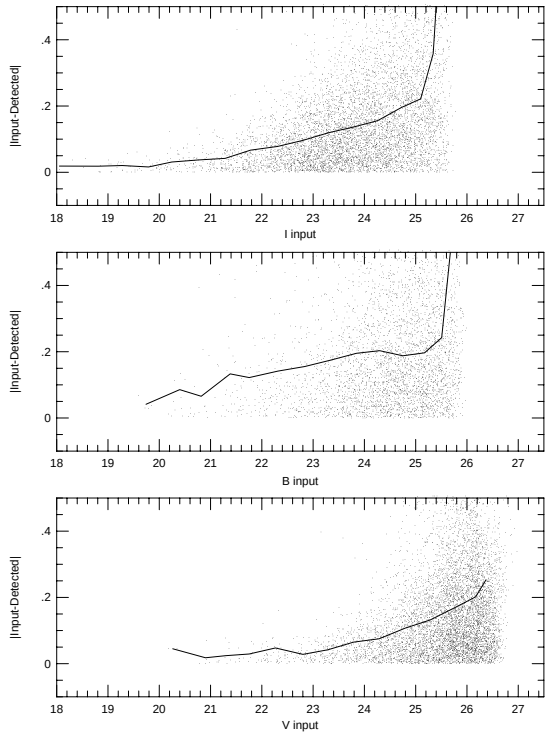

FIG. 4.—Comparison of the absolute difference between the artificial star input magnitude and the detected magnitude. The plots have been placed on the same scale as Fig. 2 for ease of comparison. The line is the average difference as a function of magnitude. This average for V and I follows the error curve in Fig. 2, indicating the random photometric errors reported by DoPHOT are accurate representations of the uncertainty. The B data appears noisier than expected. The source of this noise is unknown.

Note that the completeness is not quite 100% at intermediate magnitudes. These stars were detected, but did not pass through the matching process. The central regions of the galaxy are fairly dense, so the stars were eliminated when there was more than one star within the matching radius. This happened with real stars as well. Furthermore, the cutoff in I is steeper than in V. This is because I was the limiting magnitude for the VI CMD. Stars not detected in I were removed from the list, even though they may have been detected in V. This flattened the V cutoff. A similar effect occurred with the BV CMD, where B is the limiting magnitude.

The absolute difference between the input magnitude and the recovered magnitude for the artificial stars is plotted in Figure 4. Also plotted is a solid line showing the average of this difference. The curves for V and I follow the internal errors reported by DoPHOT. On the other hand, the B data appear to have more noise than predicted. Although we do not know the source for this extra noise, the incompleteness measurements for the B data were not crucial to our calculations.

2.3. *Comparison with Previous Measurements*

We compared our calibration with previously published ground-based measurements. There were two sets matching our filter system. AGM obtained CCD photometry in Johnson BV. HS measured CCD photometry in Johnson B and Cousins R. AGM made comparisons with previously published photometry, while HS made comparisons between their B data and AGM's. Therefore, we compared our BV data with that of AGM.

Of the 142 stars detected by AGM, we were only able to match half with stars detected in the WFPC2 images. Those that were not matched were resolved into two or more stars by *HST*. Figure 5 shows the comparison for the matched stars. The crowding difficulties also affected the accuracy of those stars that were matched, especially for faint stars. Stars fainter than $V \approx 22$ were scattered brighter than the *HST* data by up to several magnitudes on account of the overlap in stellar images.

For stars brighter than $V \approx 22$, there is a linear relation with unity slope; however, with an offset. The formal zero-point offset is 0.27 in V and 0.19 in B, where the AGM data is brighter in both cases. HS found the AGM B data to be brighter by 0.17 mag, consistent with our calibration.

Calibrating ground-based stellar photometry in galaxies at this distance is difficult and uncertain. There has often been disagreement among various authors (e.g., AGM). The standard sources provide an accurate calibration for the data. But, if individual stars in the target galaxy are compared, large zero-point differences can be found, because the photometry of an individual star is made inaccurate by crowding. Differences in the seeing, as well as the measurement techniques, introduce systematic differences in the photometry. The range in zero points found among various groups ($\sim$0.2; AGM) is a good indication for the size of these systematic errors.

There were no standard observations with which to calibrate the *HST* data directly. Therefore, we had no means to determine which of the ground-based calibrations was most accurate. Given these uncertainties, we believed the Holtzman transformations to be the most reliable calibrations for this data set.

3. PHYSICAL PARAMETERS

In order to compare the data to stellar evolution models, we must have accurate estimates for the distance, reddening, and metallicity of the stellar population. Each of these is discussed below.

From our data we could estimate the distance based on the tip of the RGB. From the RGB luminosity function (Fig. 6) we measured the tip to be at $I = 22.70 \pm 0.15$. Lee, Freedman, & Madore (1993) gave $M_I = -4$ for the RGB tip, which implies a distance modulus of 26.7. This agrees extremely well with the Cepheid distance of 26.75 ± 0.35 determined by Tolstoy et al. (1995). The effects of metallicity on the Cepheid calibration are expected to be small. Tolstoy et al. (1995) used the LMC for calibration, which is $\sim$8 times as metal-rich as GR 8. Based on the metallicity dependence found by Kennicutt et al. (1998), this amounts to a 0.2 shift further away in distance modulus. This is smaller than the quoted errors; therefore, we adopted the Cepheid distance modulus of 26.75 for the present work.

The area of the galaxy was needed to normalize the SFR calculations. Since nearly the entire galaxy fits into our field of view, we wanted to use a standard diameter. Following Hunter & Gallagher (1986), we used the Holmberg diameter (Holmberg 1958), which is 2.'0. At the adopted distance, this gives an area of 5.3 kpc^2.

GR 8 is at a high Galactic latitude (76°) with a low metallicity, so the Galactic foreground and internal reddening corrections were expected to be small. The reddening maps of Burstein & Heiles (1984) indicated Galactic reddening of $E(B-V) = 0.007$. De Vaucouleurs et al. (1991) estimated the Galactic extinction at $E(B-V) = 0.009$ and the inter-

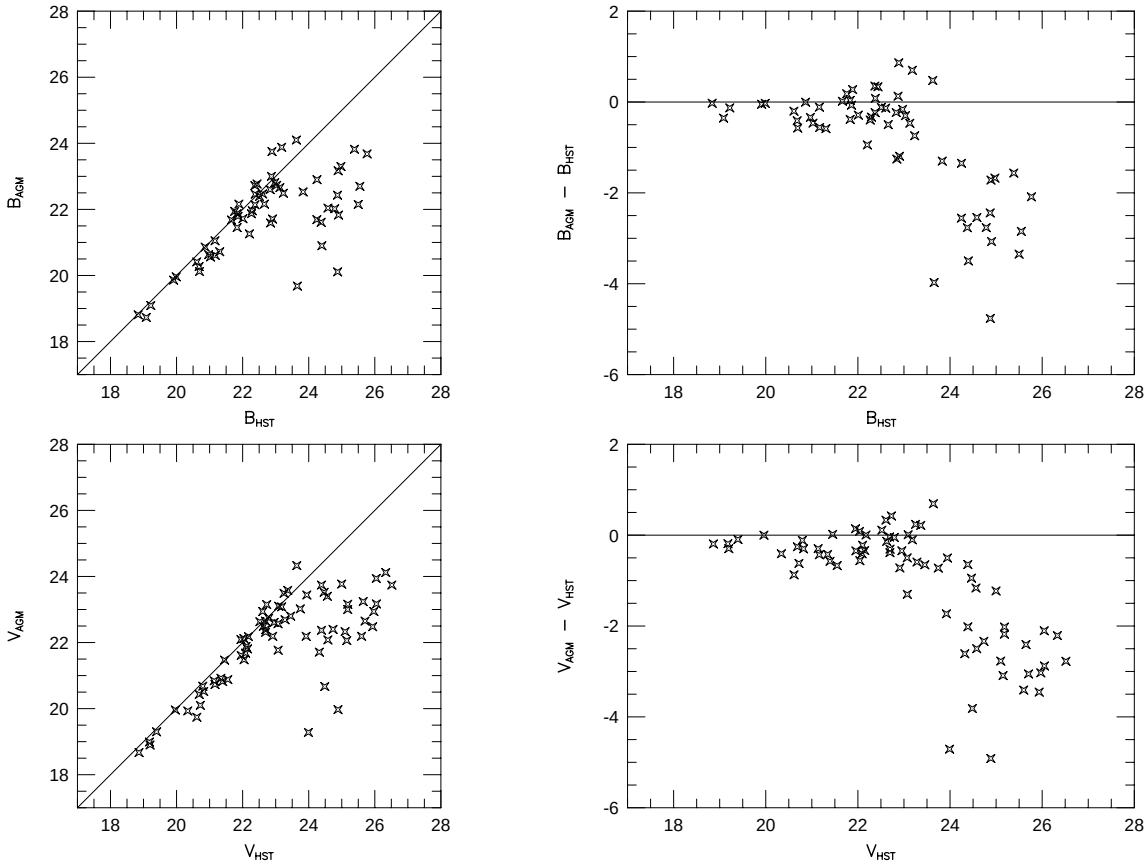

FIG. 5.—Comparison of AGM magnitudes with our data. Of the 142 AGM stars, we were only able to match half with our data. Those that did not match were resolved into two or more stars by *HST*. The agreement brighter than ~22 is good, with a small zero-point offset. The fainter stars of AGM are scattered up to several magnitudes brighter than the *HST* data. This arises because of the difficulty with crowding faced by ground-based imaging of galaxies at this distance.

nal extinction at $E(B-V) = 0.005$. We adopted $E(B-V) = 0.014$, to include the internal extinction. Assuming $R_V = 3.3$, the conversions of Cardelli, Clayton, & Mathis (1989) gave extinction ratios $A_B/A_V = 1.326$ and $A_I/A_V = 0.485$. Based on this, the extinction corrections were $A_B = 0.06$, $A_V = 0.05$, and $A_I = 0.02$. These corrections were applied to the data presented in this paper. As a check on this reddening value, we compared theoretical isochrones with the color-color diagram (see § 4.1).

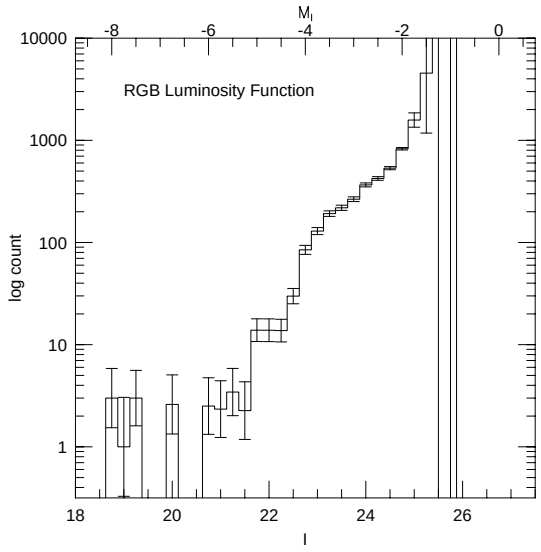

FIG. 6.—RGB luminosity function. The bins are 0.25 mag wide. They have been corrected for incompleteness. The errors reflected both Poisson counting statistics and errors from the incompleteness correction. We have estimated the tip of the RGB to be at $V = 22.70 \pm 0.15$.

The nebular oxygen abundance has been measured to be ~5% of the Solar value (Moles et al. 1990). This should reflect the chemical composition of the gas from which the youngest stars formed. Since we were primarily concerned with the youngest stars (<1 Gyr old), we adopted this as the stellar metallicity ($Z = 0.001$).

4. CMDS AND MODEL COMPARISONS

4.1. *Photometry Results*

Figures 7–9 show the CMDs and color-color diagram. The photometry was corrected for reddening as discussed in § 3. 1840 stars were matched in *BV*, while 4924 were matched in *VI*. Of these, 1343 stars were detected in all three filters. Approximately 60% of the stars have errors better than 0.2 mag.

The high-resolution imaging of the *HST* overcame much of the crowding difficulty that limits ground-based observations. This led to far more reliable photometry and accurate color indices. It also allowed limits that were ~3 mag fainter than can be achieved from the ground, even with a relatively small number of orbits. The increased accuracy produced highly detailed CMDs with several clearly defined populations.

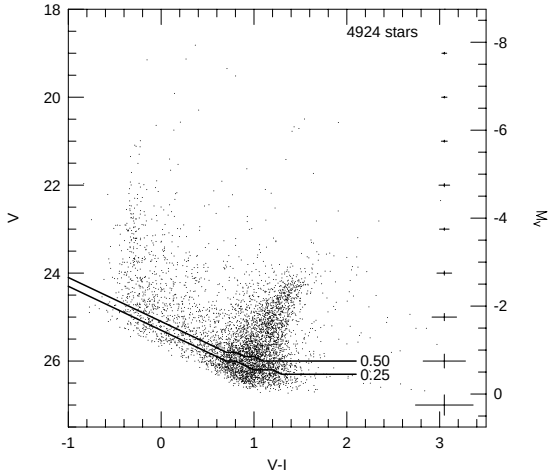

FIG. 7.—*VI* CMD for GR 8. The photometry has been corrected for reddening. Crosses at right indicate the average error at each magnitude. Thick lines indicate the completeness levels 0.25 and 0.50. The right axis shows absolute magnitude assuming a distance modulus of 26.75. The RGB and MS are the most prominent features. There is also a sparse sequence of blue HeB stars just redward of the MS, as well as the corresponding red HeB stars. Finally, there are several AGB stars.

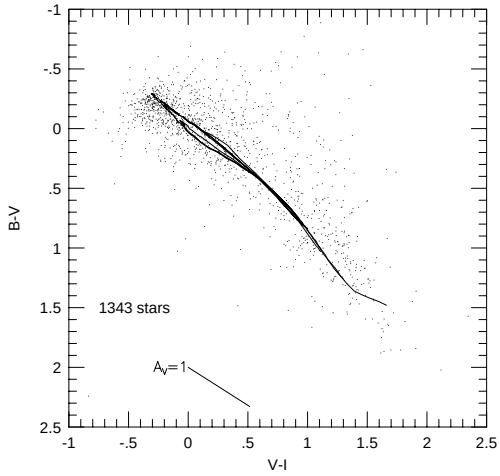

FIG. 9.—Two-color diagram for GR 8. The photometry has been corrected for reddening. Plotted in the lower left is the reddening line for $A_V = 1$. The lines plotted over the data are theoretical isochrones from Bertelli et al. (1994). They are for metallicity $Z = 0.0004$ and ages 10 Myr, 100 Myr, and 1 Gyr. The isochrones align well with the MS and blue portion of the data. The isochrones lie a little below the locus of the red portion, because $B-V$ is very incomplete for the red stars.

The red portions of the CMDs contain the RGB, and possibly the red clump at roughly $M_V = 0$ (e.g., Bertelli et al. 1994), just below the photometric limits (Fig. 7). These features were not detected in *B*. The presence of these stars is strong evidence for an underlying population at least several Gyr old. Also on the red side are possible AGB stars. At low metallicity these stars rise nearly vertically beyond the tip of the RGB. This can confuse measurements of the RGB tip magnitude. Finally, there were a handful of red supergiants belonging to a young population (10 Myr–1 Gyr).

In addition to the red populations, there is an extremely young population on the blue side of the CMDs. This young population was already known to exist from the Hα imaging (Hodge et al. 1989) and the presence of bright blue stars (Hoessel & Danielson 1983). The blue stars divide into two populations: the main sequence (MS) on the left and the blue HeB stars on the right. The MS is well-populated, and contains stars as young or younger than 10 Myr old. Blue HeB stars are core He–burning stars in the bluest extent of the so-called "blue loop" phase. This sequence is sparsely populated.

As a check on the adopted reddening correction, we compared the color-color diagram with theoretical isochrones (Fig. 9). The $Z = 0.001$ isochrones from Bertelli et al. (1994) were used. The isochrones aligned well with the MS and blue portion of the data. The isochrones lay a little below the locus of the red portion. This was because the *B* data was very incomplete for these red stars, which biased the distribution.

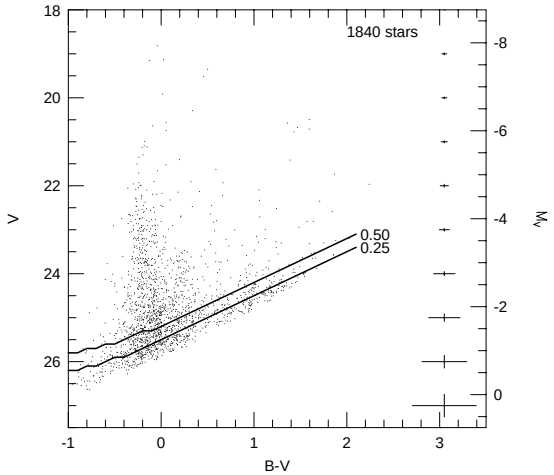

FIG. 8.—*BV* CMD for GR 8. The photometry has been corrected for reddening. Crosses at right indicate the average error at each magnitude. Thick lines indicate the completeness levels 0.25 and 0.50. The right axis shows absolute magnitude assuming a distance modulus of 26.75. The only prominent feature is the MS. The *B* exposures did not detect the RGB.

4.2. *Detection of a Halo*

Since the galaxy covered only WF3 and WF4, stars detected in WF2 could be used to estimate contamination by Galactic field stars. We used only the half of WF2 furthest from GR 8 to try to avoid the galaxy. Thirty-six stars were detected in this region down to our photometric limits. WF3 and WF4 combined cover four times this area, so, if these were all foreground stars, we expected to find ~ 144 Galactic field stars in the *VI* CMD. The CMD for these stars is shown in Figure 10. They are primarily fainter than $V = 24$, with $0.25 < V-I < 1.5$. There are two brighter stars with $V-I \approx 0.5$.

These numbers were checked against star-count models of the Galaxy. Ratnatunga & Bahcall (1985) calculated the Galactic stellar density toward globular clusters based on the Bahcall & Soneira (1980) model. The nearest cluster to GR 8 is NGC 5272 ($l = 42°$, $b = 79°$; this is equivalent to $l = 318°$ because of symmetries in the model), which is 7.°6 away. The number of stars expected down to limiting magnitude $V = 27$ is 2.79 stars arcmin^{-2}. WF3 and WF4 combined cover 3.2 arcmin^2, so the model predicts ~ 9 Galactic stars.

The comparison field on WF2 implies 16 times the number of Galactic stars as the model predicts. The model distribution predicts 2–3 stars with $19 < V < 23$ and

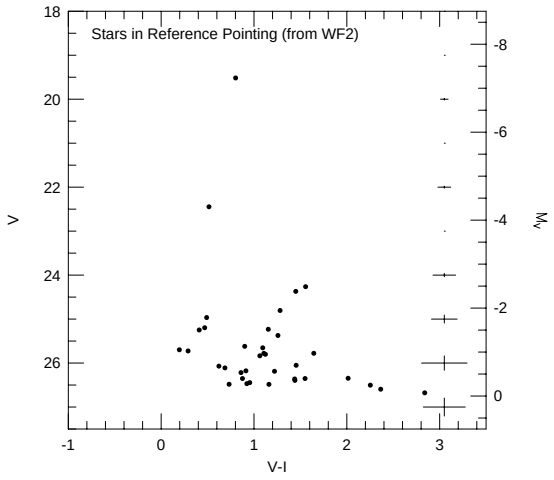

FIG. 10.—*VI* CMD of the comparison field (on WF2) used to estimate contamination by Galactic field stars. We detect 16 times more stars than models of the Galaxy predict. Further, the detected stars follow the RGB at the distance of GR 8. Therefore, we believe we have detected an extended halo at least 1.2 kpc from the center of the galaxy.

$V-I < 1.2$ along with 6–7 redder stars fainter than $V = 21$. The comparison field clearly shows the brighter, bluer stars in the right numbers. However, there are more redder, fainter stars in the comparison field than the model. Furthermore, the comparison field red stars follow the RGB distribution for the distance of GR 8.

The star-count models for stars with $V > 22$ were based on extrapolations of the luminosity function, and were not directly confirmed with observations (Ratnatunga & Bahcall 1985). This was a reasonable extrapolation, and we did not expect the uncertainty to be as large as a factor of 16, as was observed. Furthermore, the fact that the detected stars follow the RGB for the distance of GR 8 made us confident that we had detected stars associated with GR 8 in this comparison field.

The CMD distribution, and number counts of stars in the comparison field imply that we detected a low-density stellar extension, or "halo" surrounding the main body of GR 8. It extends at least 1.2 kpc from the center of the galaxy, and has a density that is ~ 100 times lower. This is not a separate component with a different density distribution. It is the tail in the exponential distribution of stars in the main body of the galaxy (see § 5). There is no evidence for such a "halo" in H I or Hα imaging. However, if the "halo" is predominantly old, as is suggested by the distribution along the RGB, we did not expect to find associated gas emission.

Although the stars detected in this field are sparse, we could roughly estimate the surface brightness of this "halo." The flux from the stars detected in this field was added, and divided by the total area of the field. The surface brightness is $V \sim 28.3$ arcmin^{-2}. It was difficult to estimate the contribution to the surface brightness from stars fainter than the photometry limit. This required assumptions for the age of the stars, as well as the IMF. However, we measured the residual surface brightness from the sky and galaxy in this field to be $V \sim 23$ arcmin^{-2}. This was the expected sky contribution (Burrows 1994). Thus, the contribution on account of faint stars must be a small fraction of the sky.

Further, the central region, RGB, stellar density is ~ 50 times as dense as the halo, while the detected portion of the halo covers ~ 10 times the area of the central region. Thus, the halo stellar mass is roughly 20% that of the central galaxy.

4.3. *Stellar Evolution Models*

For the metallicity of GR 8 we adopted 5% Solar, or $Z = 0.001$. There were two sets of modern stellar evolution models that could be used. The first was the Geneva models for $Z = 0.001$ (Schaller et al. 1992). Second was the Padua isochrones for $Z = 0.001$ (Bertelli et al. 1994). Unfortunately, the Padua group had not published evolution tracks for $Z = 0.001$. The closest models had $Z = 0.0004$ (Fagotto et al. 1994), which we used for comparison. Both sets of evolution tracks were converted from $T_{\rm eff}$ and L into Johnson BV and Cousins I using the model atmospheres of Kurucz (1992). The Padua isochrones were already published with observable parameters.

The Geneva group's stellar evolution models for $Z = 0.001$ were overlaid in the *VI* CMD (Fig. 11). Each track is labeled with the mass of the model in $M_\odot$. The models align well with the features of the observed CMD. In particular, the extremes of the "blue loops," or HeB stars, align with the blue and red supergiants. We also compared the Padua models with the observations (Fig. 12). These models align well with the observed CMD, except for the red extension of the HeB stars. The models are not quite red enough to match the brightest red supergiants. This is because the tracks were too metal-poor for the galaxy; as metallicity increases, the red end moves further redward.

To better match the metallicity, we plotted the Padua isochrones for $Z = 0.001$ over the CMD (Fig. 13). The blue HeB stars align well with the isochrones, as they do with the lower metallicity. Further, with the correct metallicity, the red supergiants also align well with the models. Finally, the location and shape of the RGB are well fit by the models. Comparison with the isochrones indicates stars of all ages. There are MS stars as young or younger than 10 Myr. At the other extreme, the RGB is several Gyr old. Finally, there are intermediate-age stars present as the HeB stars.

To further highlight the alignment of the models with the observations, Figure 14 shows the location of the MS turnoff, the blue HeB stars, and the red HeB stars (Bertelli et

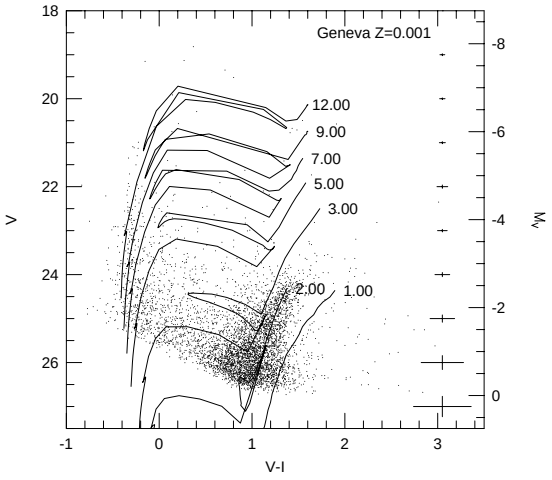

FIG. 11.—Geneva models for $Z = 0.001$ (Schaller et al. 1992) with the *VI* CMD for GR 8. The mass of each track is labeled in units of $M_\odot$. The models align well with the observed features of the CMD. In particular, the extremes of the "blue loops" align with the red and blue supergiants.

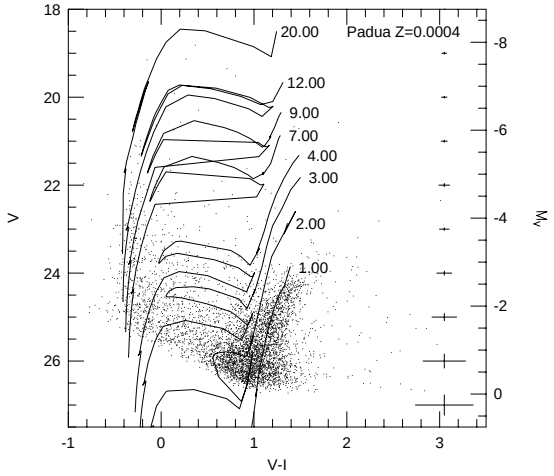

FIG. 12.—Padua $Z = 0.0004$ stellar evolution models (Fagotto et al. 1994) with the VI CMD for GR 8. The mass for each track is indicated in units of $M_\odot$. The blue end of the "blue loop" phase aligns with the observations, but the red end is too blue. This is because the models have a metallicity too low for GR 8.

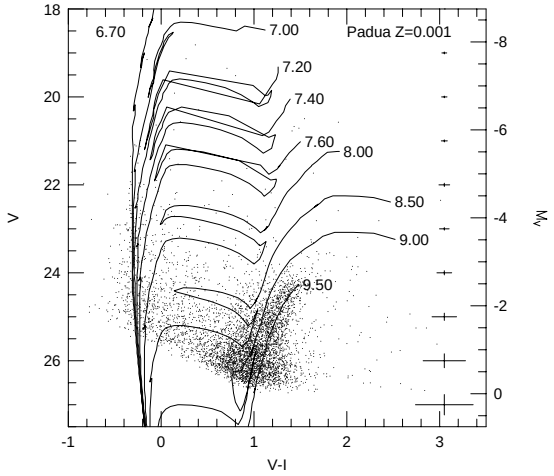

FIG. 13.—The Padua $Z = 0.001$ isochrones (Bertelli et al. 1994) with the VI CMD for GR 8. Each isochrone is labeled with the logarithm of the age. The MS aligns very well with the observations. The position of the RGB indicates the galaxy could be several Gyr old.

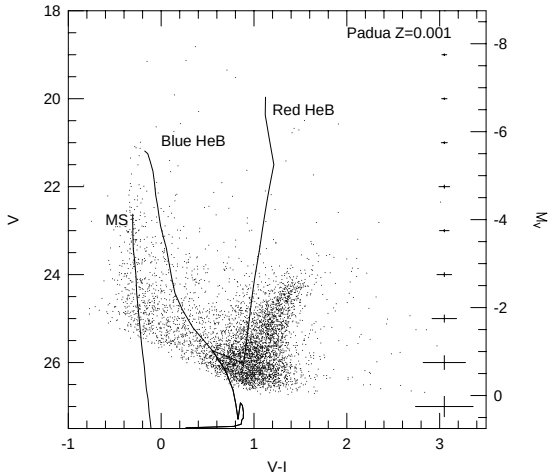

FIG. 14.—Tracks of the MS turnoff, blue HeB, and red HeB stars with the VI CMD from GR 8. The tracks come from the Padua $Z = 0.001$ isochrones (Bertelli et al. 1994). All three populations align very well with the observed distribution of stars in GR 8.

al. 1994). All three populations align very well with the model predictions.

For the purposes of this paper, any differences between the Geneva and Padua models are negligible. We were concerned with determining the SFH based on the blue HeB stars and the MS. The normalizing relations needed, including the relation between M_V and age, and M_V and mass, for both the MS and blue HeB, are nearly identical in the two models.

5. SPATIAL DISTRIBUTION

Stellar density maps were created of the main populations within GR 8. This was done by convolving the stellar position map with a Gaussian kernel. We followed the method outlined by Dohm-Palmer et al. (1997b) for correcting the odd edge shape of the WFPC2 image. For the adopted distance the pixel scale is 1.09 pc. The density maps were made with a Gaussian width of $\sigma = 20$ pixels. The area of a Gaussian beam is $2\pi\sigma^2$, so one star per beam is 335 kpc^{-2}.

Figure 15 shows the stellar density of the MS, the blue HeB, and the RGB. These three populations have very different distributions. First, the RGB, which contains the oldest stars, is spread throughout the entire galaxy. The RGB distribution extends well beyond the regions of young blue stars, H II regions, and H I gas. The density contours outside the young inner region are roughly ellipsoidal, and fall off exponentially. The outer "halo" density (see § 4.2), although sparsely populated, is consistent with the tail in this exponential distribution. These older stars have had time to respond to the overall dynamics of the galaxy, and do not reflect birth conditions.

The younger stars, on the other hand, have not moved far from their birthplace. The youngest stars, the MS, are highly concentrated into the bright blue associations, especially the lower region. These regions have long been known to be the regions of current star formation. They corresponded to the locations of H II emission (Hodge et al. 1989), as well as H I gas concentrations (Carignan et al. 1990). The star formation is definitely taking place in localized regions, and not throughout the galaxy as a whole.

The blue HeB stars have a distribution similar to the MS stars. They are located near the H II emission and gas concentrations. The central region is much more populated with blue HeB stars than the lower region. This suggests an age difference where the lower region is younger. Further, the peaks in the distribution are slightly offset from the MS peaks. The blue HeB knots seem to surround the MS knot in the lower region. The oldest blue HeB stars are $\sim$600 Myr old, while the oldest MS stars are $\sim$30 Myr old (see § 6). The offset in the blue HeB and MS distributions indicates that star formation occurred in slightly different locations, yet still within the same gas clump, over several hundred Myr.

6. RECENT STAR FORMATION HISTORY

6.1. *Main Sequence*

We started with the MS luminosity function (Fig. 16). Also plotted in Figure 16 are the MS turnoff ages based on the Padua $Z = 0.001$ models. The main feature of the luminosity function is a flattened region between 10 and 20 Myr ago. This may correspond to a decreased SFR. Further, based on the MS alone, we could only probe the history

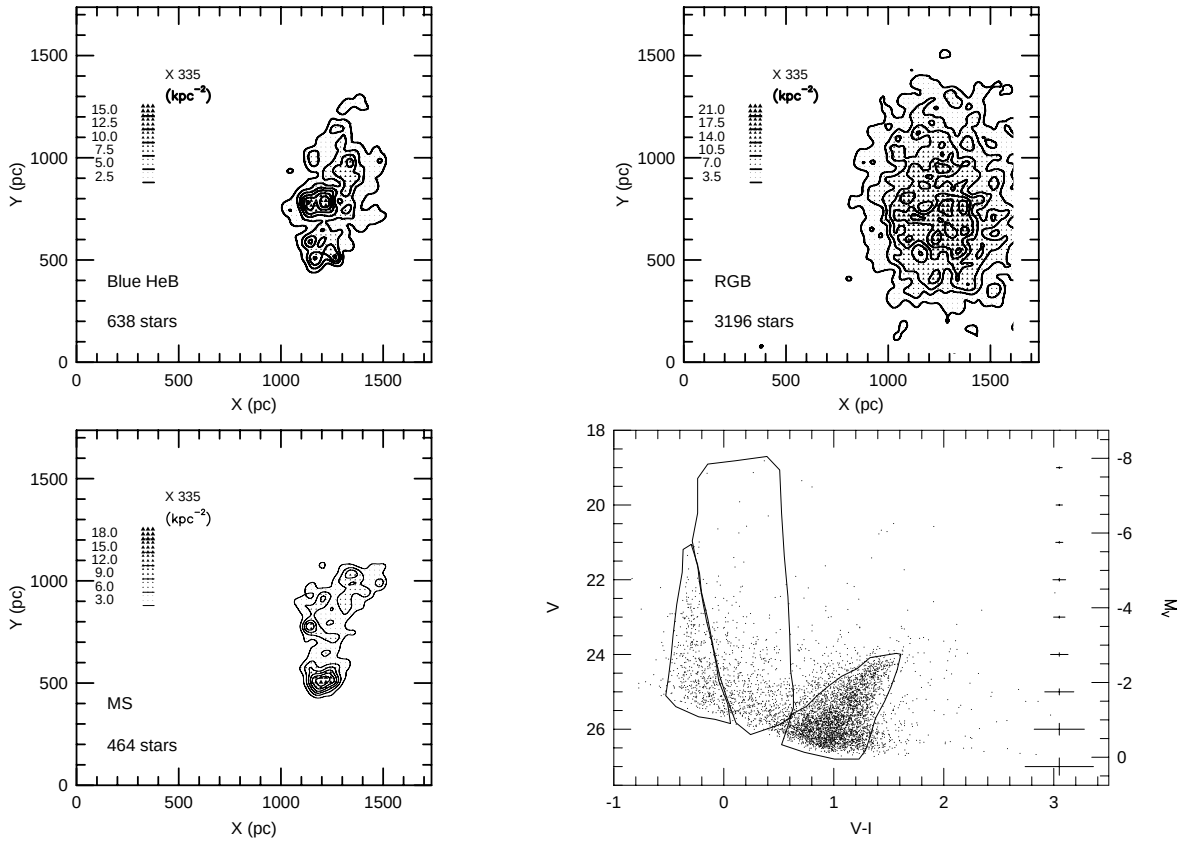

FIG. 15.—Stellar density maps for the MS, blue HeB, and RGB stars. These maps were created with a Gaussian beam with $\sigma = 20$ pixels. One star per convolution beam is 335 kpc^{-2}. The MS is highly concentrated in the bright blue associations, which is where the H II regions are also concentrated. The blue HeB stars are also strongly concentrated near the bright blue associations, but displaced slightly from the MS stars. Finally, the RGB is not concentrated in the blue associations. These stars are spread throughout the galaxy with a much more extended distribution than the younger stars. The only concentration seems to be toward the center of the galaxy.

over the past 35 Myr. Older than this, the incompleteness correction made the calculation unreliable.

Following the methods of Dohm-Palmer et al. (1997b) we calculated the SFR based on this luminosity function. This

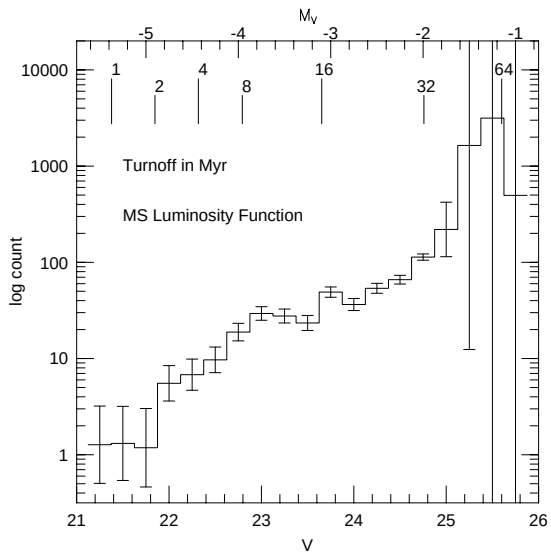

FIG. 16.—MS luminosity function. The data have been corrected for reddening and incompleteness. Bins are 0.25 mag. Errors reflect both Poisson counting noise and errors due to the incompleteness correction. Plotted above the luminosity function are the ages for the MS turnoff (Bertelli et al. 1994). Based on the MS alone, we are only able to probe the past 35 Myr.

required three relations for the MS turnoff stars: M_V versus mass, M_V versus age, and an assumed IMF. The first two came from the Padua $Z = 0.001$ evolution models. A power law was used for the IMF, and two slopes were considered: the Salpeter (1955) value ($\Gamma = -1.35$), and Scalo's (1986) value under the assumption of constant SFR in the local neighborhood ($\Gamma = -1.7$).

Unlike Dohm-Palmer et al. (1997b), we did not calculate the SFR as $M_\odot$ Myr^{-1} kpc^{-2}. This requires knowing the average initial mass (M_i), which depends on the choice of slope and functional form for the IMF. This can only be calculated correctly if the low-mass turnover is modeled. Dohm-Palmer et al. (1997b) used the Scalo function for this model, and found $M_i = 0.81\ M_\odot$ for the Salpeter slope and $M_i = 0.53\ M_\odot$ for the Scalo slope. To remove this level of uncertainty, we left the SFR in units of M_i Myr^{-1} kpc^{-2}. To compare with previous studies, $M_i = 0.8 \pm 0.3\ M_\odot$ can be used. Changing the IMF slope affected more than the value of M_i. The IMF was used directly in calculating the SFR. Changes in slope affected the luminosity function normalization. The youngest, most massive stars were the most sensitive to such changes.

The SFR based on the MS luminosity function is plotted as a function of time in Figure 17. The plotted calculation used the Salpeter slope. Given the photometric errors, 5 Myr was the shortest time to which we were sensitive. The error bars do not include systematic uncertainties of the models. A further systematic error not accounted for is the spread of the MS due to photometric errors. At the faintest

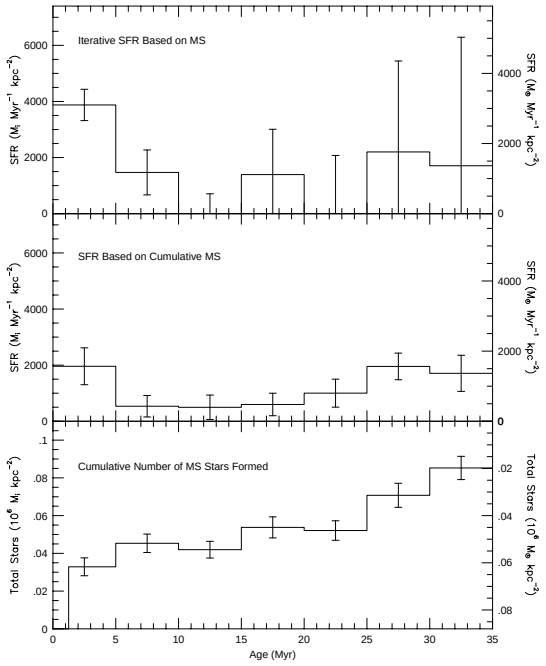

FIG. 17.—SFR of GR 8 over the past 35 Myr, based on the MS luminosity function. The bins are 5 Myr, and the data have been corrected for incompleteness. The right axis is labeled assuming $M_i = 0.8\ M_\odot$. Older than 35 Myr, the incompleteness correction is so large that the calculation is unreliable. The errors reflect both Poisson counting noise and errors from the incompleteness correction. They do not reflect any systematic errors from the assumed model. The top panel calculates the SFR based on an iterative subtraction method. The bottom panel is the cumulative mass of stars formed from the present back to the age indicated. The middle panel is the SFR calculated from the slope of the cumulative function. The youngest bin is most reliable in the iterative method. For older times, the cumulative method is more accurate.

end of the luminosity function, the photometric errors blur the MS and blue HeB stars. No correction was made for this effect.

The top panel of Figure 17 shows the SFR calculated based on an iterative subtraction of the luminosity function, starting with the youngest bin (Dohm-Palmer et al. 1997b). The bottom panel shows the cumulative number of MS stars formed at each time. The middle panel is the SFR calculated based on the slope of this cumulative function (Dohm-Palmer et al. 1997b). The two different methods are in excellent agreement. The only exception is the first bin. Since the cumulative method depends on the slope, the first bin is not accurate; however, older bins are more accurate than the iterative method.

The most recent SFR started fairly high at $\sim 3800\ M_i$ $\mathrm{Myr}^{-1}\ \mathrm{kpc}^{-2}$ ($3040\ M_\odot\ \mathrm{Myr}^{-1}\ \mathrm{kpc}^{-2}$ assuming $M_i = 0.8\ M_\odot$). Older than this it dropped to a constant level of roughly $500 M_i\ \mathrm{Myr}^{-1}\ \mathrm{kpc}^{-2}$ ($400\ M_\odot\ \mathrm{Myr}^{-1}\ \mathrm{kpc}^{-2}$). After 25 Myr it began to rise again to $\sim 2000 M_i\ \mathrm{Myr}^{-1}\ \mathrm{kpc}^{-2}$ ($1600\ M_\odot\ \mathrm{Myr}^{-1}\ \mathrm{kpc}^{-2}$). Older than this the incompleteness correction was so large that the calculation was very uncertain. For the Scalo IMF, the same general behavior was observed, except the SFR was ~ 3.5 times larger.

6.2. *Blue HeB Sequence*

We selected the blue HeB stars as shown in Figure 15. The luminosity function is presented in Figure 18. Also plotted are the ages for the blue HeB phase based on the Padua $Z = 0.001$ models. The luminosity function is relatively featureless. Based on these stars, we could probe the history back to 500 Myr, before the incompleteness correction grew too large.

Again, following Dohm-Palmer et al. (1997b), we calculated the SFR based on this luminosity function. For the blue HeB stars, this required four relations: M_V versus mass, M_V versus age, M_V versus lifetime in this phase, and the IMF. We assumed the same IMF functions as for the MS. The remaining functions were derived from the Padua isochrones for $Z = 0.001$. Because of uncertainties in the models for the most massive stars, the calculation was only reliable for ages older than ~ 20 Myr.

The SFR based on the blue HeB stars is plotted in Figure 19. This calculation assumed a Salpeter IMF. The data are binned in constant magnitude bins 0.25 wide. However, the time axis is linear. This means the bin width changes with age. This allowed us to take full advantage of the time resolution at all ages. The peak SFR occurred at roughly 50 Myr ago at a level of $800 \pm 300 M_i\ \mathrm{Myr}^{-1}\ \mathrm{kpc}^{-2}$ ($640 \pm 340\ M_\odot\ \mathrm{Myr}^{-1}\ \mathrm{kpc}^{-2}$ assuming $M_i = 0.8 \pm 0.3\ M_\odot$). The SFR then fell to $300 \pm 100 M_i\ \mathrm{Myr}^{-1}\ \mathrm{kpc}^{-2}$ ($240 \pm 110\ M_\odot\ \mathrm{Myr}^{-1}\ \mathrm{kpc}^{-2}$) by 100 Myr. There was a second peak 200 Myr ago and a minimum 325 Myr ago. This pattern may be described as a nearly constant SFR of $500 M_i\ \mathrm{Myr}^{-1}\ \mathrm{kpc}^{-2}$ ($400\ M_\odot\ \mathrm{Myr}^{-1}\ \mathrm{kpc}^{-2}$) with up to 60% deviations. For a Scalo IMF, the peak value was $1200 M_i\ \mathrm{Myr}^{-1}\ \mathrm{kpc}^{-2}$, and the nearly constant value between 100 and 500 Myr ago was ~ 1.3 times larger.

Because the blue HeB calculation was unreliable younger than 20 Myr, and the MS calculation was unreliable older then 30 Myr, there was essentially no overlap between the two calculations. Thus, we could not make a self-consistency check between the two methods. However, both methods were consistent in Sextans A (Dohm-Palmer et al. 1997b) and the Pegasus DIG (Gallagher et al. 1998), which gave us sufficient confidence in the accuracy.

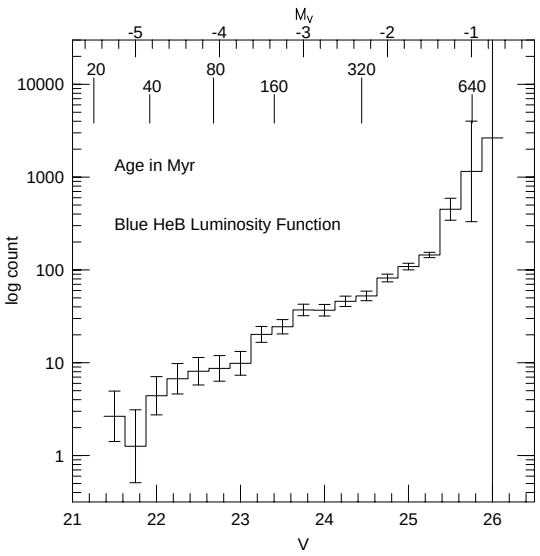

FIG. 18.—Blue HeB luminosity function. The data have been corrected for reddening and incompleteness. Bins are 0.25 mag. Errors reflect both Poisson counting noise and errors due to the incompleteness correction. Plotted above the luminosity function are the ages for the blue HeB phase (Bertelli et al. 1994). The luminosity function is relatively featureless over the past 500 Myr. Older than this the incompleteness correction is very large.

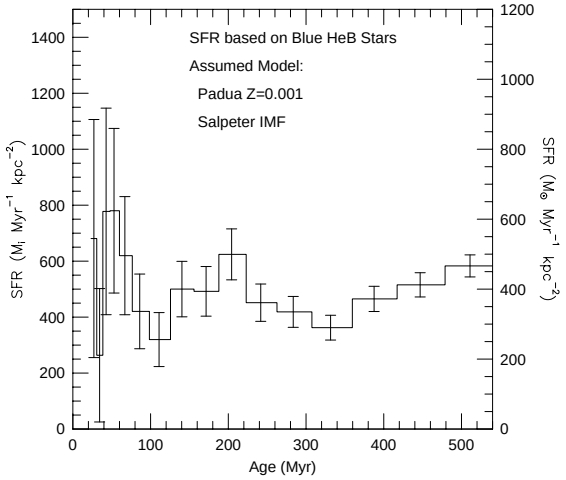

FIG. 19.—SFR of GR 8 over the past 500 Myr based on the blue HeB luminosity function. The bins are 0.25 mag, and the data have been corrected for incompleteness. The right axis has been labeled assuming $M_i = 0.8\ M_\odot$. Since the plot is linear in time, the constant magnitude bins have different widths, the shortest at the youngest age and the longest at the oldest. The incompleteness correction older than 500 Myr makes the calculation unreliable. There are two main features at 50 and 200 Myr. These are not intense episodes, only increasing by 30%–60% above a nearly constant level.

6.3. *Star Formation Patterns*

Following Dohm-Palmer et al. (1997b) we used the blue HeB stars as a tracer for the location and strength of star formation over the past 500 Myr. The blue HeB stars were binned by 10 Myr. For each bin the stars were placed in a spatial map and the SFR calculated for each location assuming a Salpeter IMF. The spatial extent was convolved with a Gaussian of $\sigma = 4''$, equivalent to 43 pc. It was also convolved in time with a Gaussian of $\sigma = 30$ Myr.

A mosaic of stills from the resulting movie is shown in Figure 20.[3] In several of the frames there are single stars outside the main body of the galaxy. This will help the reader gauge the noise level in each map. Each frame displayed is separated by 30 Myr, covering 470 to 50 Myr ago. Younger than 50 Myr, we could use the MS distribution (see Fig. 15) to identify the current location of star formation. Currently, the main region of star formation is located in the lowest red region, slightly to the left, in the 50 Myr–old frame.

The movie gives the impression that star formation occurred in small (100–200 pc) isolated regions that lasted, consistently, $\sim$100 Myr. These are a little smaller and shorter lived than the regions seen in Sextans A (Dohm-Palmer et al. 1997b). These regions are the size of super-associations, or star complexes (see review by Elmegreen 1987). These complexes often contain one or more OB associations and clusters. They are similar to the Shapley constellations (Nail & Shapley 1953) of supergiants seen in the LMC.

While they seem to dominate the appearance of the galaxy, each complex, at its peak, actually contains only 10%–20% of the total star formation in the galaxy at any given time. However, the SFR density is $\sim$10 times as large as that of the global SFR density. So the complexes in GR 8 are highly concentrated compared with the rest of the galaxy. The peak values are also $\sim$1.5 times larger than those seen in Sextans A (Dohm-Palmer et al. 1997b).

Could it be that all the stars formed in these complexes, but that over time they diffused from their birthplace? As discussed in Dohm-Palmer et al. (1997b), this is unlikely, since the dynamical lifetimes of such complexes are probably larger than the look-back times considered here. However, it should be noted that such dynamical arguments have not been well studied in the literature. More likely, stars formed throughout the galaxy with regions of enhancement that arose in response to the dynamical perturbations of the galaxy.

There is no event that peaked in exactly the same place as another. However, they do seem to be concentrated in three major areas, which corresponded to the current location of the main H I concentrations (Carignan et al. 1990). This implies that the H I clumps are long-lived features in the galaxy, and that star formation can occur in them over several hundred Myr. The star formation seems to have occurred in different locations and at different times within the same H I clump, while never destroying the clump.

There are two possible dynamical situations. First, if the galaxy is rotating as a solid body, the H I clumps, and the associated stars, would maintain the same relative positioning. On the other hand, if random motions dominate the dynamics, then the H I clumps, along with the associated stars, must be gravitationally bound to maintain their identity over these time periods. Either case implies the stellar diffusion timescale is long compared with the look-back time of 500 Myr. The most likely interpretation is that the molecular clouds that form stars are gravitationally bound, as most Giant Molecular Clouds in the Milky Way appear to be (Combes 1991). The gravitational energy holds the complex together, lengthening the stellar diffusion timescale, and allowing multiple stellar generations over several hundred Myr.

The first impression from the movie was that the star formation events appear and disappear at random times and locations with respect to one another. On the other hand, there are several clear age sequences across the galaxy. These sequences start at one end of the galaxy, pass through the center, and end at the other.

To help illuminate such a pattern, we integrated the SFR density perpendicular to the major axis of the galaxy. Figure 21 shows the integrated value as a function of time in both contours and gray scale. Also plotted are two lines indicating the slope corresponding to 10 km s^{-1}. This plot contains unmistakable diagonal features that may indicate a causal relation between neighboring regions. However, these features are not so strong as to rule out random events, especially considering the galaxy's small size. Despite this, it was worth exploring the consequences of the supposition that they were causally related.

The diagonal features can almost be connected in a sawtooth pattern, indicating a wave of star formation that is reflecting from end to end within the galaxy. Alternatively, if the galaxy is a rotating disk, the pattern may be a sinusoid, indicating the star formation is traveling around the disk. The speed of these diagonal features is roughly 4 km s^{-1}, much slower than expected if the waves are supersonic. Thus, they do not appear to be caused by shocks from supernovae. Since the diagonal features cross the entire

[3] An MPEG version of the movie can be accessed at: http://ast1.spa.umn.edu/robbie/gr8.

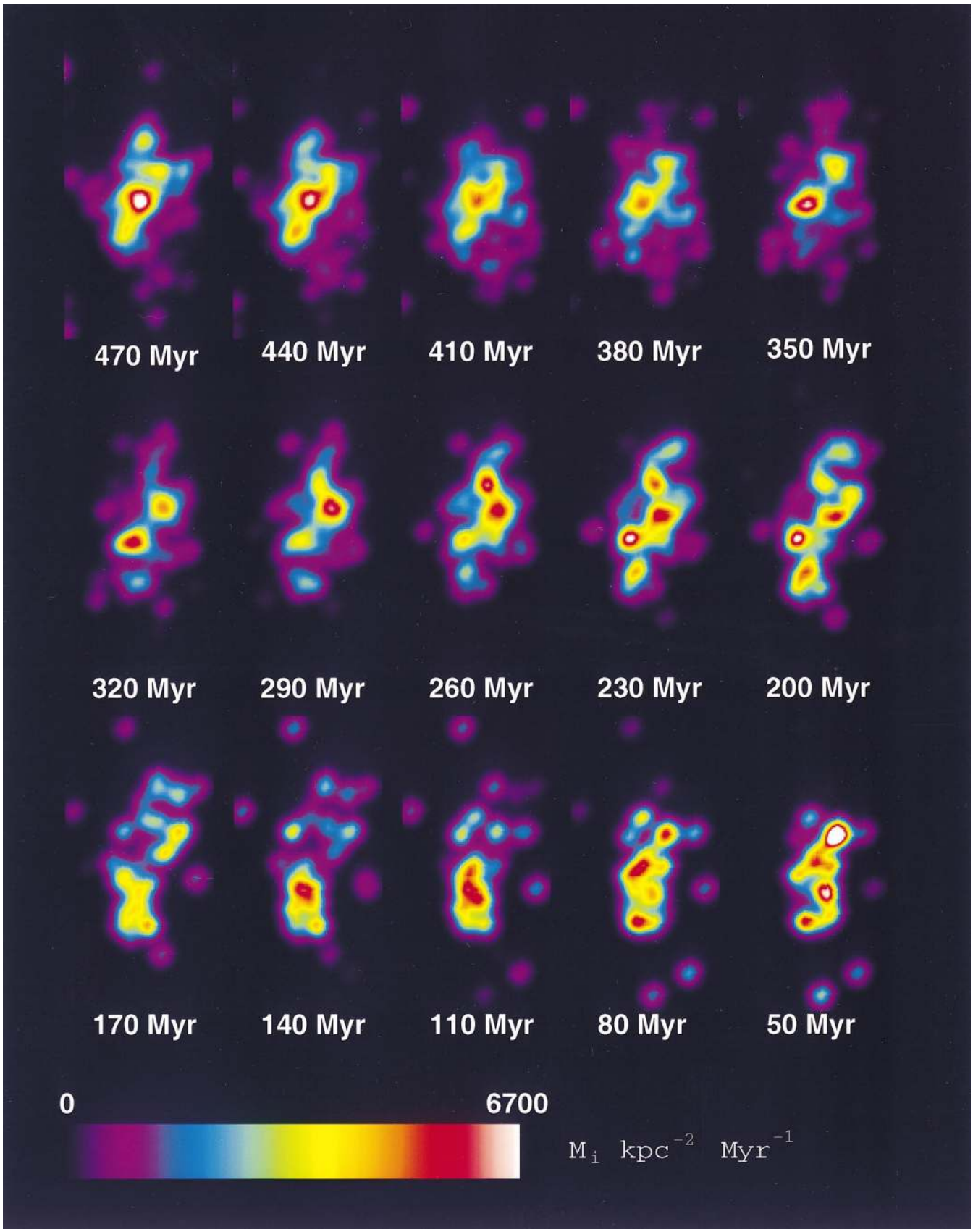

FIG. 20.—A gallery of stills from the movie showing the location and strength of star formation over the past 500 Myr. The frames are spaced by 30 Myr. The spatial extent was convolved with a Gaussian of $\sigma = 4''$, equivalent to 43 pc. It was also convolved in time with a Gaussian of $\sigma = 30$ Myr. The plots shown were created assuming a Salpeter IMF. Each frame is 0.8×1.6 kpc. The star formation occurs throughout the galaxy with smaller regions (100–200 pc) of concentrated star formation. These concentrated regions last ~ 100 Myr and come and go in different locations and different times with no discernible patterns. However, the star-forming regions do seem concentrated near the main H I clumps, implying that that these structures must last several 100 Myr.

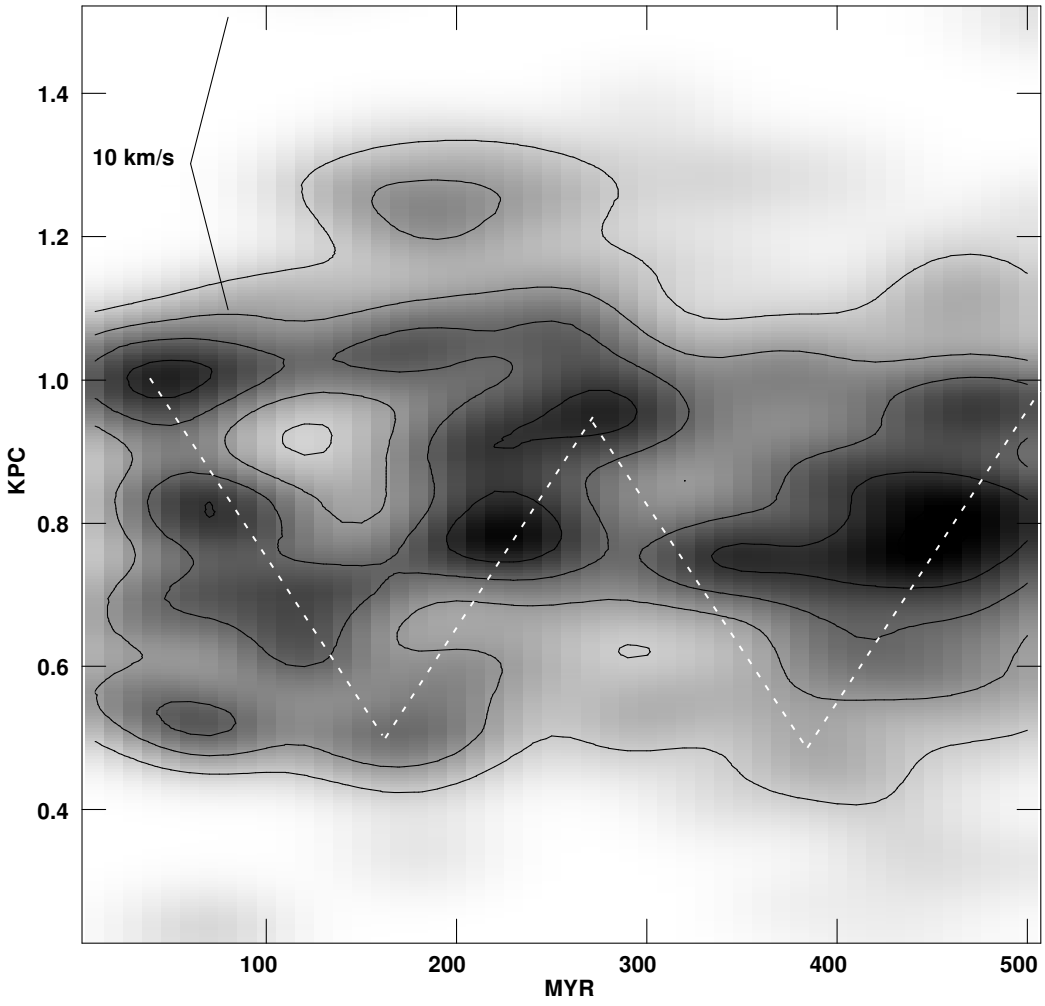

FIG. 21.—SFR as a function of time and position along the major axis. The SFR is shown in both contours and gray scale. The SFR was integrated over the direction perpendicular to the major axis. In the upper left are lines indicating the slope that corresponds to 10 km s^{-1}. The enhanced regions of star formation occur in clumps, but there is some indication that there may be a wave that triggers these clumps passing back and forth through the galaxy. We have indicated the passage of this possible wave with a dashed line. This line corresponds to ~ 5 km s^{-1} in all cases.

galaxy, they are more likely caused by the overall dynamics, responding to the gravitational potential of the galaxy.

The diagonal features are not smooth and continuous. Rather, they have knots of enhanced star formation in particular locations (Fig. 21). As noted above, these enhancements occur near the current locations of H I concentration. If there is some kind of wave passing through the galaxy, it must only induce star formation in regions where conditions are ripe. Thus, as the wave encounters a high-density gas complex, a star formation event is triggered. However, regions between the H I concentrations inspire little or no star formation.

We estimated the efficiency of star formation by comparing the total stellar mass formed in each complex with the H I column density. The average SFR/area in a star-forming complex is $\sim 5700\ M_i$ Myr^{-1} kpc^{-2}. The area of such a complex is ~ 0.05 kpc^{-2}, and they last ~ 100 Myr. So the total mass formed is of order 23,000 $M_\odot$, assuming $M_i = 0.8\ M_\odot$. The H I column density is $\sim 10^{21}$ $cm^{-2} = 8 \times 10^6\ M_\odot$ kpc^{-2}. For the area of the star-forming complexes, the total mass is $4 \times 10^5\ M_\odot$. Assuming this is a typical H I density, the efficiency of star-forming complexes is $\sim 6\%$. This is similar to the value found for Sextans A.

In summary, the star formation occurs throughout the galaxy with smaller complexes (100–200 pc) of concentrated star formation. These concentrated regions last ~ 100 Myr and lie on or near the current locations of the H I peaks. This implies the star-forming regions are long-lived, and may be gravitationally bound. Furthermore, the star formation may be triggered by some form of wave traveling through the galaxy. Finally, we estimated the star-forming efficiency in these complexes to be $\sim 6\%$.

7. DISCUSSION

7.1. *Comparison with Previous Studies*

Previous studies used very different distance estimates for GR 8. To make direct comparisons, we needed to adjust for this difference. This was difficult to do precisely, but crude adjustments were made.

Based on CCD stellar photometry in g and r (Thuan & Gunn 1976), Hoessel & Danielson (1983) estimated the time since the last major episode of formation to be 11 Myr. Adjusted for their distance of 25.6, this actually corresponds to ~ 3 Myr. This is consistent with our data. Because of low number counts for the brightest stars, we can only say that stars formed within the last 5 Myr.

AGM used UBV stellar photometry to study the star

TABLE 3

SUMMARY OF GALAXY PROPERTIES

	D (Mpc)	d_{25} (kpc)	M_B^0	$B-V$	$L_{H\alpha} \times 10^{36}$ (ergs s^{-1})	$M_{H\,I}/L_B$ ($M_\odot/L_\odot$)	12 + log (O/H)	References
Sex A	1.4	2.4	−13.91	0.26	1000	1.4	7.49	1, 2, 3, 4, 5
GR 8	2.2	0.69	−12.12	0.38	2	0.76	7.63	2, 6, 7, 8
Peg DIG.....	0.76	1.1	−11.43	0.54	2	0.47	7.93	2, 9, 10, 11, 12
Leo A	0.69	1.0	−11.52	0.26	1	1.3	7.30	2, 5, 13, 14, 15

REFERENCES—(1) Sakai, Madore, & Freedman 1996; (2) de Vaucouleurs et al. 1991; (3) Hunter & Plummer 1996; (4) Skillman et al. 1988b; (5) Skillman et al. 1989; (6) Tolstoy et al. 1995; (7) Carignan et al. 1990; (8) Hodge et al. 1989; (9) Gallagher et al. 1998; (10) Hunter, Hawley, & Gallagher 1993; (11) Lo et al. 1993; (12) Skillman, Bomans, & Kobulnicky 1997; (13) Tolstoy et al. 1998; (14) Strobel, Hodge, & Kennicutt 1991; (15) Young & Lo 1996.

formation history. They adopted 25.0 for the distance modulus. They described the present star formation as not intense, and that the blue color of the galaxy came primarily from stars 17 to 30 Myr old. This was a natural consequence of the closer distance. Using the Cepheid distance modulus of 26.75, these ages correspond to 2–10 Myr. Thus the current star formation is actually higher than their estimate. They gave a value of $\sim 40 M_i$ Myr^{-1} kpc^{-2}, after applying the Holmberg area normalization. We could roughly correct this value by adjusting the IMF and MS turnoff age for the further distance. A shift of 1.75 in magnitude implies a shift of Δ log mass $= -0.3$, and Δ log age $= 0.8$. For the IMF slope adopted by AGM (-1.8), this gives a total correction of 19. So the adjusted SFR is $760 M_i$ Myr^{-1} kpc^{-2}. This is lower than we found for the past 10 Myr by a factor of 5. However, since this was a crude adjustment, the agreement is not unsatisfactory.

Wyatt & Dufour (1993) estimated the ages for the three main regions of current star formation based on *UBVRI* stellar photometry from WF/PC-1 images. They found an age sequence where the northernmost region was 75 Myr old, the central region was 40 Myr old, and the southeast region was 15 Myr old. However, they used the closer distance modulus of 25.0. We found the same age sequence, except, with the further distance, the ages were roughly 23, 10, and 6 Myr old, respectively. Wyatt & Dufour described this as a wave of star formation, implying causally linked events. This is similar to the impression given by our movie (Fig. 21), where a wave traveled back and forth between the ends of the galaxy. The wave described by Dufour & Wyatt would then be the most recent pass. The sequence is consistent with the movie that ended at 20 Myr with the upper (northernmost) region being active.

Finally, Tolstoy (1995) analyzed the stellar population using Thuan-Gunn (Thuan & Gunn 1976) *r*, *g*, & *i* photometry. The CMDs were compared statistically with Monte Carlo models using Bayesian inference (Tolstoy & Saha 1996). The best-fitting model was a decreasing SFR that was 5 times higher 1 Gyr ago than the present. However, it was noted that "none of the models give a particularly great match." The SFH calculated in this paper does not extend fully to 1 Gyr, but stops 500 Myr ago. However, the SFH over this time period is most consistent with a constant SFR. If anything, the present value is higher than 300 to 500 Myr ago (Fig. 19). There is some hint that the SFR is rising older than 400 Myr; however, we could not reliably extrapolate to ages older than 500 Myr to determine if this trend continues. Thus, we could not rule out the conclusion of Tolstoy, but did not see such a trend during the past 500 Myr.

7.2. *Comparison with Other Local Group dI's*

We compared our results with three other dI galaxies that were a part of our program: Sextans A, Pegasus DIG, and Leo A. Table 3 lists several relevant parameters for these galaxies. Figure 22 shows the SFR/area for all four galaxies over the past 500 Myr. Sextans A consistently has the highest SFR/area, followed by Leo A. Pegasus and GR 8 have very similar SFRs/area, which were consistently lower than the other two.

There are several noteworthy features. First, the Hα luminosity is much higher for Sextans A than it is for the others. The Hα emission is in response to the very youngest star formation (<3 Myr; Hunter & Gallagher 1986), which is far higher in Sextans A than in the other three galaxies.

Second, there is a trend with $M_{H\,I}/L_B$. The higher the gas mass–to–stellar mass fraction is, the higher the average SFR/area. This was expected. Assuming a similar star-forming efficiency for all dI's, the more gas that is contained in the galaxy, the higher the rate of star formation.

Third, there were no large bursts in the recent past of any of the galaxies. Even the most recent event in Sextans A jumped only a factor of 3 in SFR/area. There were no bursts with strength matching that of the blue compact starburst galaxies, which have an SFR ranging from roughly 10^4 to 10^7 $M_\odot$ Myr^{-1} (see review by Thuan 1991). With the four

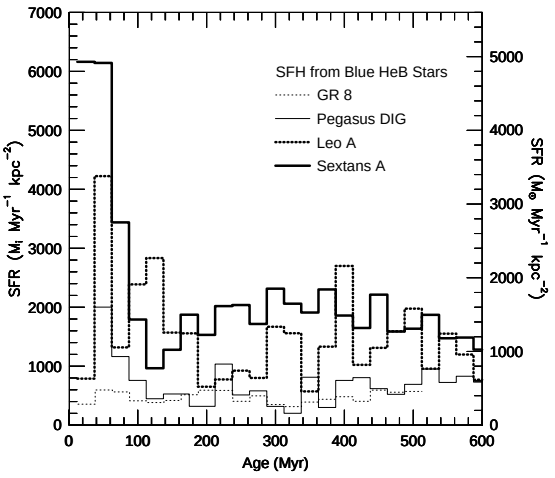

FIG. 22.—Star formation history of four nearby dI galaxies based on the blue HeB luminosity function. Bins are 25 Myr. The right axis has been labeled assuming $M_i = 0.8$ $M_\odot$. Sextans A consistently has the highest SFR/area, followed by Leo A. Pegasus and GR 8 have a very similar SFR/area, which is consistently lower than in the other two galaxies.

galaxies combined, our observations cover 2 Gyr of the recent past. Assuming a burst length of 100 Myr (NGC 1569; Vallenari & Bomans 1996), we observed no bursts during 20 possible burst episodes. We concluded that such strong bursts in the current epoch are rare, occurring in less than 5% of dI galaxies. This statistic is based on few galaxies, and observations of more galaxies are needed.

Finally, the star formation process is very similar in all four galaxies. We made movies similar to that of GR 8 and Sextans A (Dohm-Palmer et al. 1997b) for both Pegasus and Leo A. They all showed that the star formation occurs at a low level throughout the galaxy, with regions of enhancement that are of order 100 pc across and last of order 100 Myr. The distribution of current star formation in dI galaxies hinted at this pattern (e.g., Hunter & Gallagher 1986), although such indicators, including Hα and bright blue stars, are only sensitive to timescales of a few Myr.

7.3. *Summary*

HST WFPC2 imaging allowed very accurate photometry measurements of the stellar population. The high-resolution images overcame much of the crowding difficulties faced by typical ground-based imaging. The resulting CMDs show several well-defined populations. There is a very young MS (<10 Myr), with the corresponding blue and red supergiant stars. Further, there is a well-populated RGB as old or older than several Gyr. These features align well with stellar evolution models of the appropriate metallicity.

We estimated the tip of the red giant branch to be at $I = 22.7 \pm 0.15$, implying a distance modulus of 26.7. This is in excellent agreement with the Cepheid determination of 26.75 ± 0.35.

Based on the RGB distribution, we found evidence for a low-density halo that extends to at least 1.2 kpc, well beyond the H I extent of the galaxy. The young MS stars are found in bright blue complexes, reflecting the distribution of their birth. These complexes are near the highest density H I clumps and H II regions. The massive evolved blue HeB stars are also located in small dense regions near H I clumps, but are slightly offset in space from those of the MS. Since the blue HeB stars are older, on average, by 10 to several hundred Myr, these offset clumps are the location of older star formation events.

Our calculation of the global SFH for GR 8 was based on the MS and blue HeB luminosity functions. The MS allowed us to probe the past 30 Myr, while the blue HeB stars extended the calculation to 500 Myr. During this time the SFR/area is fairly constant, at $500 M_i$ Myr^{-1} kpc^{-2} (400 $M_\odot$ Myr^{-1} kpc^{-2} assuming $M_i = 0.8\ M_\odot$) with up to 60% deviations.

The blue HeB stars were used as a tracer for the location and strength of star formation over the past 500 Myr. The star formation occurs in superassociation-size regions (100–200 pc), which last $\sim$100 Myr. The star formation may occur in response to some form of wave traveling through the galaxy. The star-forming complexes concentrate in the current locations of H I clumps. This suggests that the H I clumps are long-lived features that support several star-forming events over several 100 Myr. The most likely explanation is that these complexes are gravitationally bound. The star-forming efficiency of these complexes was estimated to be $\sim$6%.

We compared our results with those of three other dI galaxies: Sextans A, Pegasus DIG, and Leo A. A trend of higher SFR with larger $M_{\rm H\,I}/L_B$ was found. Further, the star formation process is similar in all four galaxies, consisting of low-level global star formation with complexes of enhanced star formation $\sim$100 pc across that last $\sim$100 Myr. Finally, none of the four dI galaxies contained a large starburst, comparable to those in BCD galaxies. This implies that such large bursts are relatively rare in the current epoch, and that BCDs undergo a different evolution than normal dI's.

We thank the referee for comments. We would like to thank Fred Lo for his insights into the gas dynamics, and Don Garnett for sage advice. R. C. D.-P. thanks the University of Minnesota Graduate School for a Doctoral Dissertation Fellowship. This work was partially supported by NASA grants STScI/GO-5915, NAGW-3189, and NAG 5-3373.

REFERENCES

Aparicio, A., García-Pelayo, J. M., & Moles, M. 1988, A&AS, 74, 375 (AGM)
Babul, A., & Ferguson, H. C. 1996, ApJ, 458, 100
Bahcall, J. N., & Soneira, R. M. 1980, ApJS, 44, 73
Bertelli, G., Bressan, A., Chiosi, C., Fagotto, F., & Nasi, E. 1994, A&AS, 106, 275
Burrows, C. J., ed. 1994, Wide Field and Planetary Camera 2 Instrument Handbook (Baltimore: STScI)
Burstein, D., & Heiles, C. 1984, ApJS, 54, 33
Campos, A. 1997, ApJ, 488, 606
Cardelli, J. A., Clayton, G. C., & Mathis, J. S. 1989, ApJS, 345, 245
Carignan, C., Beaulieu, S., & Freeman, K. C. 1990, AJ, 99, 178
Colless, M., Ellis, R. S., Broadhurst, T. J., Taylor, K., & Peterson, B. A. 1993, MNRAS, 261, 19
Combes, F. 1991, ARA&A, 29, 195
de Vaucouleurs, G., de Vaucouleurs, A., Corwin, H. G., Jr., Buta, R. J., Paturel, G., & Fouqué, P. 1991, Third Reference Catalog of Bright Galaxies (New York: Springer)
de Vaucouleurs, G., & Moss, C. 1983, ApJ, 271, 123
Dohm-Palmer, R. C., et al. 1997a, AJ, 114, 2514
———. 1997b, AJ, 114, 2527
Elmegreen, B. G. 1987, in Star Forming Regions, ed M. Peimbert & J. Jugaku (Dordrecht: Reidel), 457
Fagotto, F., Bressan, A., Bertelli, G., & Chiosi, C. 1994, A&AS, 104, 365
Gallagher, J. S., III, & Hunter, D. A. 1986, AJ, 92, 557
Gallagher, J. S., Tolstoy, E., Dohm-Palmer, R. C., Skillman, E. D., Cole, A. A., Hoessel, J. G., Saha, A., & Mateo, M. 1998, AJ, 115, 1869
Groth, E. J. 1986, AJ, 91, 1244
Hodge, P. W. 1974, PASP, 86, 645
Hodge, P., Lee, M. G., & Kennicutt, R. C., Jr. 1989, PASP, 101, 640
Hoessel, J. G., & Danielson, G. E. 1983, ApJ, 271, 65
Hoffman, G. L., Salpeter, E. E., Farhat, B., Roos, T., Williams, H., & Helou, G. 1996, ApJS, 105, 269
Holmberg, E. 1958, Medd. Lunds Astron. Obs., Ser. II, No. 136
Holtzman, J. A., Burrows, C. J., Casertano, S., Hester, J., Trauger, J. T., Watson, A. M., & Worthey, G. 1995, PASP, 107, 1065
Hopp, U., & Schulte-Ladbeck, R. E. 1995, A&AS, 111, 527 (HS)
Hunter, D. A., & Gallagher, J. S., III. 1986, PASP, 98, 5
Hunter, D. A., Hawley, W. M., & Gallagher, J. S. 1993, AJ, 106, 1797
Hunter, D. A., & Plummer, J. D. 1996, ApJ, 462, 732
Kennicutt, R., et al. 1998, ApJ, 498, 181
Koo, D. C., & Kron, R. G. 1992, ARA&A, 30, 613
Kurucz, R. L. 1992, in Stellar Populations of Galaxies, ed. B. Barbuy & A. Renzini (Dordrecht: Kluwer), 225
Lee, M. G., Freedman, W. L., & Madore, B. F. 1993, ApJ, 417, 553
Lo, K. Y., Sargent, W. L. W., & Young, K. 1993, AJ, 106, 507
Moles, M., Aparicio, A., & Masegosa, J. 1990, A&A, 228, 310
Moss, C., & de Vaucouleurs, G. 1986, PASP, 98, 1282
Nail, V. M., & Shapley, H. 1953, Proc. Natl. Acad. Sci., 39, 358
Patterson, B., Wyatt, R. J., & Dufour, R. J. 1993, Rev. Mexicana Astron. Astrofis., 27, 165
Ratnatunga, K. U., & Bahcall, J. N. 1985, ApJS, 59, 63
Reaves, G. 1956, AJ, 61, 69
Saha, A., Sandage, A., Labhardt, L., Tammann, G. A., Macchetto, F. D., & Panagia, N. 1996, ApJ, 466, 55
Sakai, S., Madore, B. F., & Freedman, W. L. 1996, ApJ, 461, 713

Salpeter, E. E. 1955, ApJ, 121, 161
Scalo, J. M. 1986, Fundam. Cosmic Phys., 11, 1
Schaller, G., Schaerer, D., Meynet, G., & Maeder, A. 1992, A&AS, 96, 269
Schechter, P. L., Mateo, M. L., & Saha, A. 1993, PASP, 105, 1342
Skillman, E. D. 1996, in ASP Conf. Ser. 106, The Minnesota Lectures on Extragalactic Neutral Hydrogen, ed. E. D. Skillman (San Francisco: ASP), 208
Skillman, E. D., Bomans, D. J., & Kobulnicky, H. A. 1997, ApJ, 474, 205
Skillman, E. D., Kennicutt, R. C., & Hodge, P. W. 1989, ApJ, 347, 875
Skillman, E. D., Kobulnicky, H. A., & Dohm-Palmer R. C. 1998, in preparation
Skillman, E. D., Melnick, J., Terlevich, R., & Moles, M. 1988a, A&A, 196, 31
Skillman, E. D., Terlevich, R., Teuben, P. J., & van Woerden, H. 1988b, A&A, 198, 33
Spaans, M., & Norman, C. A. 1997, ApJ, 483, 87
Strobel, N. V., Hodge, P., & Kennicutt, R. C. 1991, ApJ, 383, 148
Thuan, T. X. 1991, in Massive Stars in Starbursts, ed. C. Leitherer, N. R. Walborn, T. M. Heckman, & C. A. Norman (Cambridge: Cambridge Univ. Press), 183
Thuan, T. X., & Gunn, J. E. 1976, PASP, 88, 543
Tolstoy, E. 1995, Ph.D. thesis, Univ. Groningen
Tolstoy, E., et al. 1998, AJ, 116, 1244
Tolstoy, E., & Saha, A. 1996, ApJ, 462, 672
Tolstoy, E., Saha, A., Hoessel, J. G., & Danielson, G. E. 1995, AJ, 109, 579
Tyson, J. A. 1988, AJ, 96, 1
Vallenari, A., & Bomans, D. J. 1996, A&A, 313, 713
van den Bergh, S. 1959, Publ. David Dunlap Obs., 2, 147
Verter, F., & Hodge, P. 1995, ApJ, 446, 616
Wyatt, R. J., & Dufour, R. J. 1993, RMA&A, 27, 213
Young, L. M., & Lo, K. Y. 1996, ApJ, 462, 203